Diversity Image Restoration with Dynamically Changing Magnification, Rotation, and Translation

David R. Gerwe, Brad Eucker, Carlos Luna
Boeing Directed Energy Systems, Los Angeles, CA
Brandoch Calef
Boeing Laser Technical Services, Kihei, HI

Abstract

A generalization of diversity algorithms for image restoration and wavefront sensing is presented that allows joint processing of image sets in which the sampling geometry relating focal plane array pixels to their projected positions onto the target is different for each frame. The geometric relations are assumed to be well approximated by affine transformations embracing translation, rotation, skew, and magnification, but not higher order distortions such as pincushion or as resulting from 3D parallax issues. This work extends diversity image processing methods such as blind deconvolution and phase diversity in which the wavefront or PSF is jointly estimated with the object allowing these algorithms to be applied to collection engagement with 3D dynamic motion between the sensor and target. Simulations demonstrate the approach for ground-to-space and air-to-ground applications. A regularization approach is used to balance image sharpening against noise amplification and to handle spatial variations in effective sample density across the composite FOV.

1. INTRODUCTION

Image processing techniques such as multi-frame blind deconvolution (MFBD), phase diversity (PD), phase diverse phase retrieval (PDPR), and supersampling algorithms, combine the information contained in a set of image frames to produce a restored image of improved quality and/or information about the imaging system such as estimates of the wavefront aberrations or PSF.[1-18] These methods belong to the broader class of diversity algorithms which make use of the richer information content available in from multiple images of an object each collected under different conditions. Typically the underlying object is assumed to be unknown but static and effectively identical for all images in the set. Common diversity mechanisms and their corresponding algorithm types include use temporal fluctuations of the point spread function (PSF) for MFBD, known differences in the wavefront aberrations of the optical system for PD and PDPR, and differences in the sampling geometry of the optical image by a focal plane array (FPA) for supersampling[†]. Diversity differences can be controlled and deliberate such as in use of a defocused sensor channel for phase diversity or microscan motion for superresampling or the differences may be from random causes such as line-of-sight jitter and atmospheric turbulence. Uncontrolled diversity typically requires estimation of extra nuisance parameters associated with the random variations in collection conditions.

The total information content of the diversity image set is higher than that of a single image. This is more than just an effective SNR increase from multiple identical measurements with different noise realizations. Rather the measurement diversity increases the ratio of constraints to unknowns improving the invertibility of the inverse problem to be solved. This class of algorithms is an active area of research and has shown strong success for mitigating image quality degradation effects including wavefront aberrations from imperfections and limitations in

[†] In this paper the term supersampling is used to refer to methods that produce a higher resolution image on a grid with finer sample density measurement than an input sequence of measured images that are undersampled and aliased relative to the optical cutoff associated with the system transfer function of the combined blur associated with diffraction and pointing jitter. This is also referred to as superresolution in the literature. The term supersampling is used in this paper to avoid confusion with the other common use of superresolution to refer to recovery of image frequency components beyond the optical diffraction limit.

the optical system, boundary layer air flow, and extended path turbulence, pointing jitter and motion smear, and undersampling/aliasing of the imaging resulting from a coarsely pixelated FPA.

The most popular methods for solving the diversity inverse problem are based on estimation theoretic principles that determine the unknown object and collection/degradation parameters by finding the values that jointly attain the best agreement with the measured data, the image formation physics, noise statistics, and any *a priori* statistics or constraints on the object and collection parameters. Most of the published literature for blind image restoration algorithms that jointly estimate the PSF address translational image registration but not unknown rotation, skew, magnification or higher level distortions[1-10]. Conversely much of the work in supersampling addresses frame-to-frame sampling geometry differences often including higher order distortions and intra-image object motion but typically assumes the PSF is static and known[11-18]. The focus of this paper is on extending estimation-theoretic methods for diversity image processing to handle image sets with geometry differences that can be approximated as an affine transformation. Other papers that have investigated this extension have placed sharp limitations on the extent of the PSF, e.g. its support, and on the complexity of its spatial structure[18-19]. In this work we demonstrate the ability to treat cases of PSFs with large extent and complex speckle structure resulting from strong wavefront aberrations. Section 2 describes the mathematical approach. Illustrative examples of its application for MFBD, PD, and supersampling are presented in Section 3.

2. Approach

The majority of diversity image processing algorithms discussed in the literature can be derived from estimation theoretic principles. The object and/or wavefront or PSF is parameterized in terms of a set of variables, and their estimates are defined by the joint set of values that maximize the agreement between a forward model of the image formation chain and the set of image measurements. This forward model relates the parameters to the image that would be measured in the absence of noise. Several common variations of the formal definition of *maximal agreement* are used such as maximum likelihood (ML), penalized ML, maximum *a posteriori* (MAP), and minimum mean square error (MMSE). All derive from the probability density function associated with the noise mechanisms of the measurement and additional constraints or statistical expectation regarding the object and other unknown system parameters. This subject is well covered in the literature[2,3,8]. The main elements of the forward model used in this paper are illustrated through the following equation.

$$g_j(x) = S(\Lambda_j)\, P(\theta_j)\, S(\Xi_j)\, o(z) + n_j(x) \tag{1}$$

$$I_j(x) = g_j(x) + n_j \tag{2}$$

In this equation, o is the object common to all images, $j=1\text{-}J$ indexes the set of images I_j, $P(\theta_j)$ represents the PSF associated with image j as parameterized by the vector θ_j, and n_j is the measurement noise. The expected value of the images, which is equivalent to the image that would be acquired in the absence of noise is given by g_j, and the actual measured noisy image data by I_j. The sample points on the grid for the object and the image are indexed by z and x respectively. S represents an interpolation operator which re-samples a spatial quantity from one evenly spaced rectilinear grid to another. In this paper the relationships are assumed to be well-represented by an affine transformation parameterized by rotation, horizontal and vertical scale magnification, skew, and translation. Eq. (1) includes two affine transformations. The first is parameterized by the vectors Ξ_j and corresponds to the transformation of the target plane grid coordinates to a new rectilinear grid associated with the target's appearance as viewed from the sensor or telescope pupil plane. This transformation is performed before blurring and image sampling. The second transformation is parameterized by the vectors Λ_j, occurs after application of image blur, and models the sampling geometry of the FPA including aliasing effects, optical zoom, sensor rotation (such as occurs when using a telescope with a Coudé path), and tilt of the FPA with respect to the optical axis. Including both pre- and post-blur affine transformations in the model provides complete generality to accurately treat target→sensor→FPA geometry and sampling density differences. Eqs. (1-2) are easily generalized to address optical system phenomena such as spectral and polarization dependencies, FPA flat-field and gain, and intra-exposure dynamics[9]. These, are however, beyond the focus of this paper and will be ignored so as not to add tedious and unwarranted complexities.

The affine interpolation operation uses 2D sinc interpolation performed as described by Granrath et. al. [16] using the discrete fractional Fourier transform[21]. This treatment is both mathematically rigorous and numerically

efficient. Care must be taken in choosing grid densities for the object and intermediate quantities to ensure that that the treatment does not induce non-physical aliasing. Judicious choice of grid spacing also enables FPA aliasing to be directly and rigorously treated in the Fourier domain by folding and summing aliased frequency components. The finite rectangular shape and size of the detector pixels is treated through multiplicative sinc() terms in the optical transfer function (equivalent to convolution of the optical PSF by a 2D rect function).

The cost function is derived from a modified Poisson noise model used to approximate the combined effects of detector read noise, quantization, and photon shot noise.[20-21] Noise between different pixels and images is assumed to be statistically independent. This results in the following probability density function,

$$p(I|\theta,o) = \Pi_{\{j,x\}}\ [g_j(x|\theta_j,o) + \sigma^2_j(x)]^{I_j(x)}\ \exp[-(g_j(x|\theta_j,o) + \sigma^2_j(x))]\ /\ [I_j(x) + \sigma^2_j(x)]! \qquad (3)$$

where $\Pi_{\{j,x\}}$ indicates the product of terms for all pixel values x and all image frames $j=1\text{-}J$. The symbol '!' indicates factorial, and $\sigma^2_j(x)$ is the Gaussian read noise variance for image j pixel x. The reader should note that the expected value of the image $g_j(x|o, \theta_1 \ldots \theta_J)$ is a function of the unknown object and PSF parameters, where in equation (3) the use of θ without subscript denotes the concatenation of all vectors θ_j into a single vector. In this paper the object is simply parameterized in terms of radiance values on a rectilinear grid and the PSF is parameterized in terms of the coefficients of a Zernike decomposition of an unknown wavefront aberration for each frame.

3. **Results**

The results of the approach are demonstrated through three examples illustrating the union of multi-geometry diversity to Multi-Frame Blind Deconvolution (MFBD), Phase Diversity (PD), and sampling diversity (often referred to as superresolution). All cases are performed using simulated image data. In the examples, each image of the processed set has been modeled as acquired from a series of evolving geometric changes between the target, optical system, and FPA. The instantaneous geometry is described in terms of the location of the projection of the optical system line-of-sight to the target plane (e.g. the aimpoint), slant range, relative azimuth and elevation angles between sensor and target, rotation angle of the sensor about its line-of-sight, sensor magnification (zoom) setting, and the rotational orientation and translational position of the FPA relative to the optical boresight. Image translation (aim point jitter) was treated as unknown and jointly estimated with the object and wavefront parameters, while all other geometry parameters were treated as being accurately known.

The reader should note that in all examples the targets were treated as being perfectly flat. In reality, targets exhibit topological 3D structure that would result in changes in appearance from different geometries as a result of parallax. Lighting and BRDF effects from changing geometries are also ignored. The fact that these additional complexities are not being addressed will limit successful application of the algorithm to image sets in which variability in the elevation and azimuth angle are such that the object is essentially identical for all images. Conditions that violate this restriction will result in decreased performance. Note that aim point translation and sensor rotations have no effect on object appearance and will not cause parallax or lighting effect issues. To better illustrate the described method of extending estimation theoretic algorithms to address geometry diversity, the presented examples include exaggerated geometry variations which would likely cause parallax issues.

Figure 1 demonstrates the use of the affine transformation model with MFBD processing to produce a restored image from a sequence of 10 images collected with dynamically evolving image geometry including a 45º, 200º, and 6% changes in elevation angle, azimuth angle and range respectively. Image quality is primarily limited by the degrading effects of the wavefront aberrations which were fairly severe, different for each image frame, and treated as unknown quantities that were jointly estimated. The sampling Q defined as the ratio of the diffraction angle (wavelength/aperture diameter) to IFOV (pixel width / focal length) is 2 corresponding to Nyquist sampling. The improvement in resolution of the restored image relative to the measured image sequence is dramatic. Figure 2 indicates that the restored image is arguably superior to the diffraction limit. The authors suspect that this is not a result of recovery of spatial frequencies beyond the diffraction limit, but an accurate recovery and amplification of spatial frequency components below the diffraction limit to match their amplitudes and phases in the pristine object. Because the diffraction limited image suffers from significant attenuation of spatial frequencies near to the

diffraction limit, the restored image is shaper in appearance. The reader should also note that MFBD has estimated the shape and distribution of the PSFs at a coarse structural level. Figure 3 shows similar results but with a satellite target instead of terrestrial.

Next the case in which image resolution is primarily limited by coarse camera pixelization is considered. A sequence of 20 images that are 4× undersampled relative to the diffraction limit are processed. The blur degradation is minimal. The pristine object and a subset of the degraded images set is shown in Figure 4. Also shown is the PSF correctly scaled relative to the measured images. As seen in Figures 5 and 6 the variation in the alignment of the sampling grid to the target provided by the multiple collection geometries provides a diversity of information needed to recover an image with resolution commensurate or even arguably better than the diffraction limit. It is interesting to see in Figure 6 that the resolution is best near the center of the restored image but degrades toward the edge. The center of the restored image lay within the composite FOV of all 20 measured images. However, differences in collection geometry resulted in variations in the projection of the camera FOV onto the target such that pixels increasingly far from the center of the restored image fell within the FOV of fewer and fewer of the images in the set. High resolution restoration relies on the diversity of information provided by multiple measurements of a local region on the object with different sampling alignments. To produce a fully restoration of an image region to diffraction limited quality image using N× undersampling data, requires at a minimum N^2 images that cover the desired region. This is directly related to obtaining a number of measurements equal to the number of unknowns. In practice a higher number of images is desirable to improve the condition number associated with a matrix representation of the multi-image forward model so as to mitigate inversion sensitivity and associated artifacts and noise amplification. As the number of images fused to form a region of the restored image falls below N^2, quality degrades. The use of a smoothness constraint (implemented as described in [10,22]) facilitates a graceful degradation with coverage by fewer than N^2 images, low SNR, and poor PSF quality.

Finally in Figure 7, accurate wavefront estimation is demonstrated using the multi-geometry extension of phase diverse to process images collected with different geometries. In practice the true wavefront will contain structural features at scales finer than that represented in the modal decomposition used by the estimation algorithm. As such the simulate data was produced using a decomposition including the 1st 80 Zernike modes (i.e. through 12 order), while Phase Diversity only estimated the 1st 36 (i.e. through 8th order). A wavefront aberration level of 1.8 waves rms was used (corresponding to aperture diameter to Fried parameter (D/r_o) ratio of 4.4). Multiple trials indicated wavefront estimation accuracy on order of .02-.035 waves rms. The restored image is also shown to be of much better quality than the in-focus input. It is interesting to note, that the regularization penalty employed causes the restored image to asymptote to a value related to the mean of the input images at locations that fall outside the FOV of the in- and de-focus image.

4. **Summary**

A generalized forward model was developed able to treat in tandom multiple types of image collection diversity. In particular this paper marries a capability to jointly address geometric diversity (changes in the sensor-target geometry of the image collection and changes in optical zoom and FPA rotation and tilt) with traditional diversity variations including deliberate induced or random wavefront aberrations, time varying PSF evolution, wavelength differences, and telescope aperture differences. Simulations demonstrated the use of diversity techniques such as MFBD, PD, and superresolution to counter image blur and undersampling effects to achieve image reconstructions of diffraction limited quality and accurate PSF and wavefront estimations using image sets with multiple tandom mixes of collection diversity including geometry changes that could be well approximated within an affine transformation. Furthermore this processing was able to jointly estimate PSFs of large extent and complex structure.

5. **Acknowledgements**

The authors would like to acknowledge partial support for this research provided by the United States Air Force Research Laboratory through contract FA9451-05-C-0257.

6. **References**

1. T. J. Schulz, B. E. Stribling, and J. J. Miller, ‘‘Multiframe blind deconvolution with real data: Imagery of the hubble space telescope,’’ Opt. Express **1**(11), 355-362 (1997).
2. T. J. Schulz, ‘‘Multiframe blind deconvolution of astronomic images,’’ J. Opt. Soc. Am. A 10(5), 1064-1073 (1993).
3. D. R. Gerwe, J. D. Barchers, and D. J. Lee, “Supersampling Multiframe Blind Deconvolution Resolution Enhancement of Adaptive Optics Compensated Imagery of Adaptive Optics Compensated Imagery of Low Earth Orbit Satellites,” Opt. Eng. **41**(9), 2239-2251 (2002).
4. J. C. Christou, ‘‘Blind deconvolution post-processing of images corrected by adaptive optics,’’ Proc. SPIE **2534**, 226–234 (1995).
5. D. W. Tyler, S. D. Ford, B. R. Hunt, R. G. Paxman, M. C. Roggemann, J. C. Rountree, T. J. Schulz, K. J. Schulze, J. H. Seldin, D. G. Sheppard, B. E. Stribling, W. C. van Kampen, and B. M. Welsh, ‘‘Comparison of image reconstruction algorithms using adaptive optics instrumentation,’’ Proc. SPIE **3353**, 160-171 (1998).
6. S. M. Jefferies and J. C. Christou, ‘‘Restoration of astronomical images by iterative blind deconvolution,’’ Astrophys. J. **415**, 862–874 (1993).
7. J.-M. Conan, T. Fusco, L. M. Mugnier, and F. Marchis, ‘‘Mistral: myopic deconvolution method applied to ADONIS and to simulated VLT-NAOS images,’’ ESO Messenger 99, 38-45.
8. R. G. Paxman, T. J. Schulz, J. R. Fienup, “Joint estimation of object and aberrations by using phase diversity,” J. Opt. Soc. Amer. A. **9**(7), 1072-1085 (1992).
9. D. R. Gerwe, B. H. Calef, J. Hill, and C. E. Luna, “Impact of Model Mismatch on GEMINI and AEOS Image Recovery,” AMOS Technical Conference Proceedings, (2004).
10. D. Gerwe, J Stone, C. Luna, B. Calef, “Comparison of Maximum-Likelihood Image and Wavefront Reconstruction using Conventional Image, Phase Diversity, and Lenslet Diversity Data,” SPIE Proc. **6307** 213-225 (2006).
12. M. Elad, Y. Hel-Or, “A Fast Super-Resolution Reconstruction Algorithm for Pure Translational Motion and Common Space-Invariant Blur” IEEE Trans. Img. Proc. **10**(8), 1187-1193 (2001).
13. S. Farsiu, M. D. Robinson, M. Elad, P. Milanfar, “Fast and Robust Multiframe Super Resolution” IEEE Trans. Img. Proc. **13**(10) 1327-2344 (2004).
14. H. Stark and P. Oskoui, “High-resolution image recovery from image-plane arrays, using convex projections,” JOSAA Vol. **6**(11) 1715-1726 (1989).
15. R. Fransens, C. Strecha, L. Van Gool, ”A probabilistic approach to optical flow based super-resolution,” IEEE Proc. Comp. Vision and Pattern Recog. 191-191 (2004).
16. D. Granrath and J. Lersch, “ Fusion of images on affine sampling grids,” JOSAA **15**(4) 791-801 (1998).
17. R. C. Hardie, K. J. Barnard, J. G. Bognar, E. E. Armstrong, and E. A. Watson, “High-resolution image reconstruction from a sequence of rotated and translated frames and its application to an infrared imaging system,” Opt. Eng. **37**(1) 247–260 (1998).
18. A. N. Rajagopalan and V. P. Kiran “Motion-free superresolution and the role of relative blur,” JOSAA **20**(11) 2022-2032 (2003).
19. D. L. Snyder, C. W. Helstrom, A. D. Lanterman, M. Faisal, and R. L. White, ‘‘Compensation for readout noise in CCD images,’’ J. Opt. Soc. Am. A **12**(2), 272–283 (1995).
20. D. R. Gerwe, J. L. Hill, P. S. Idell, “Cramér-Rao Analysis of Orientation Estimation: Influence of Target Model Uncertainties," JOSA A **20**(5), 817-826 (2002).
21. D.H. Bailey and P.N. Swarztrauber, "The fractional Fourier transform and applications," SIAM Rev. 33, 389-404 (1991).
22. D. R. Gerwe, M. Jain , B. Calef, and C. Luna, “Regularization for Non-Linear Image Restoration Using a Prior on the Object Power Spectrum,” SPIE Proc. **5896** 21-36 (2005).

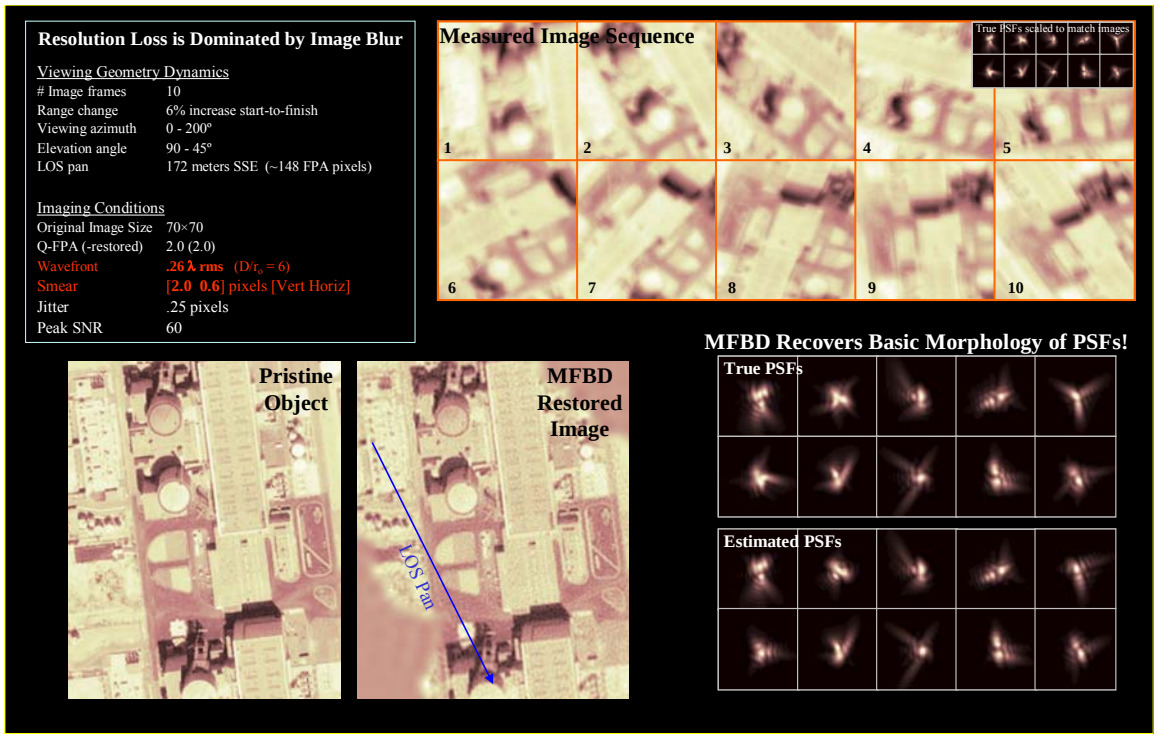

Figure 1. MFBD demonstration with time-variant imaging geometry.

Figure 2. Comparison of Multi-Geometry MFBD restored image quality to original measured data and the diffraction limited image shows recovery of at least if not better than diffraction limited quality.

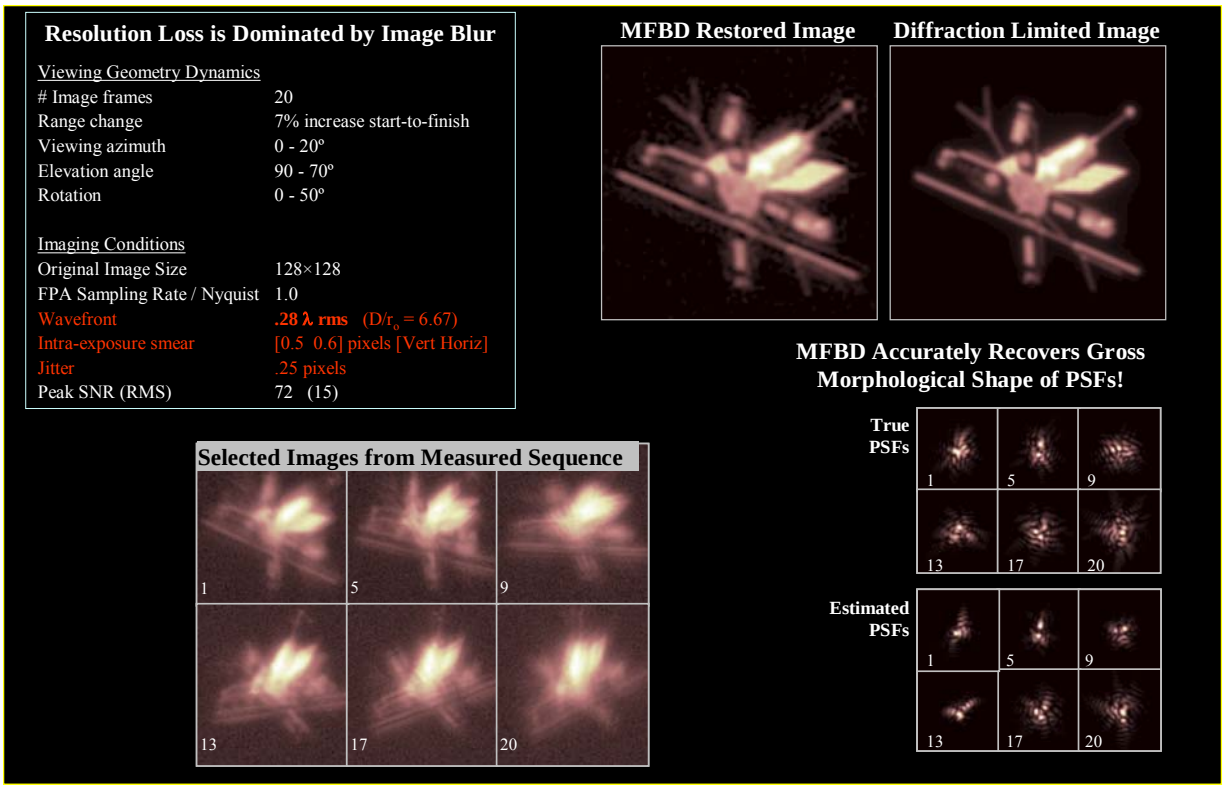

Figure 3. Demonstration of MFBD with dynamically varying geometries to a satellite target.

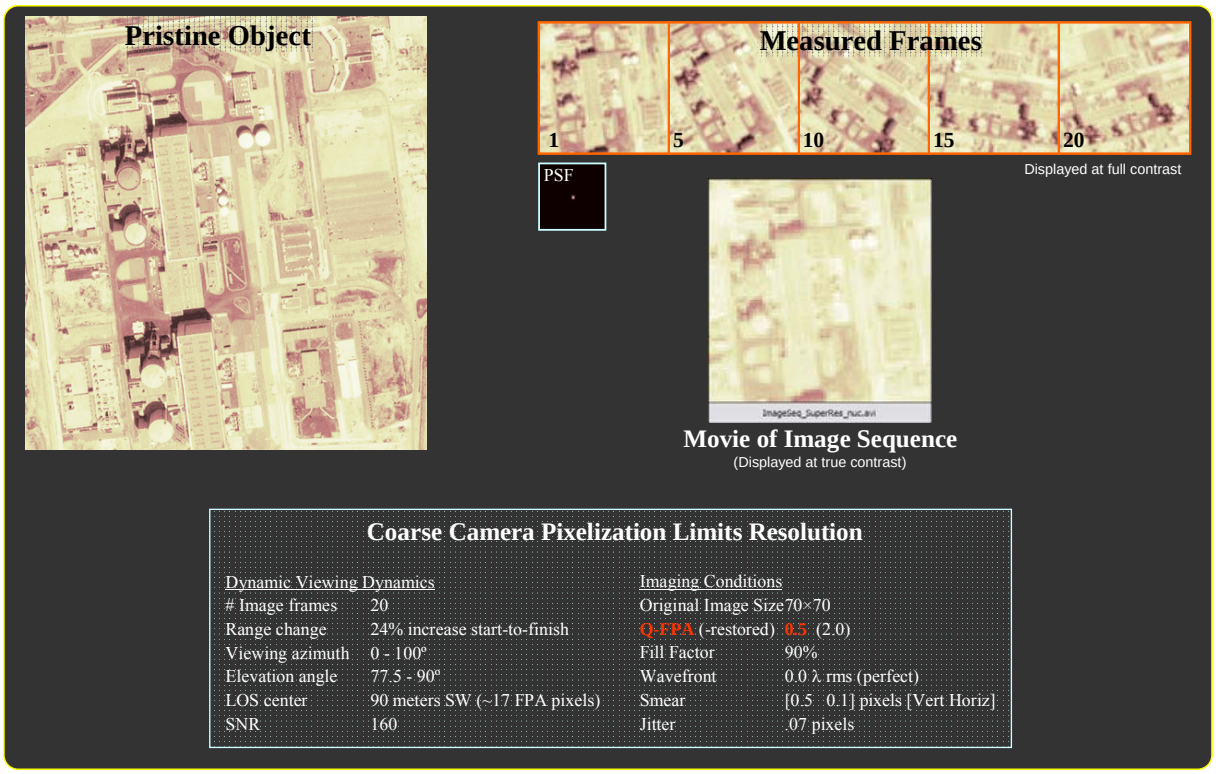

Figure 4. Pristine object and subset of 4x undersampled sequence of images used to demonstrate supersampled (superresolution) reconstruction shown in Figure 5.

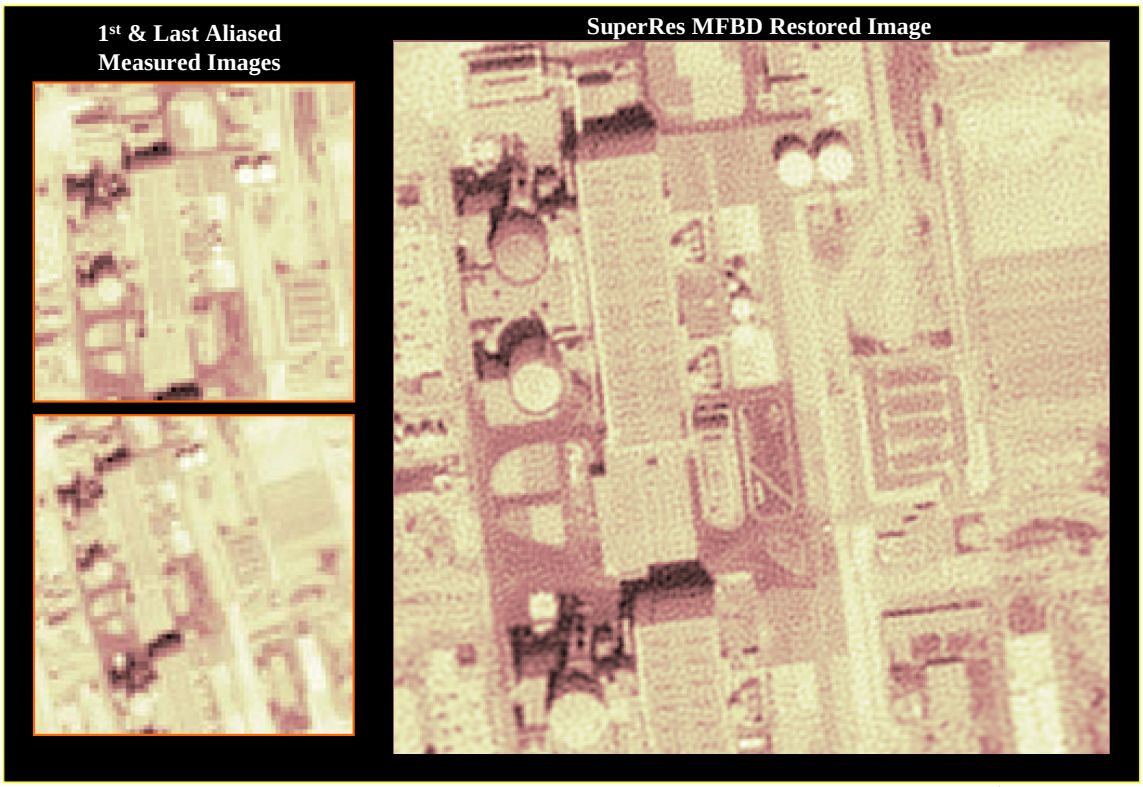

Figure 5. Comparison of the supersampling restored (superresolved) image to the 1st and last image of the input set shown in Figure 4.

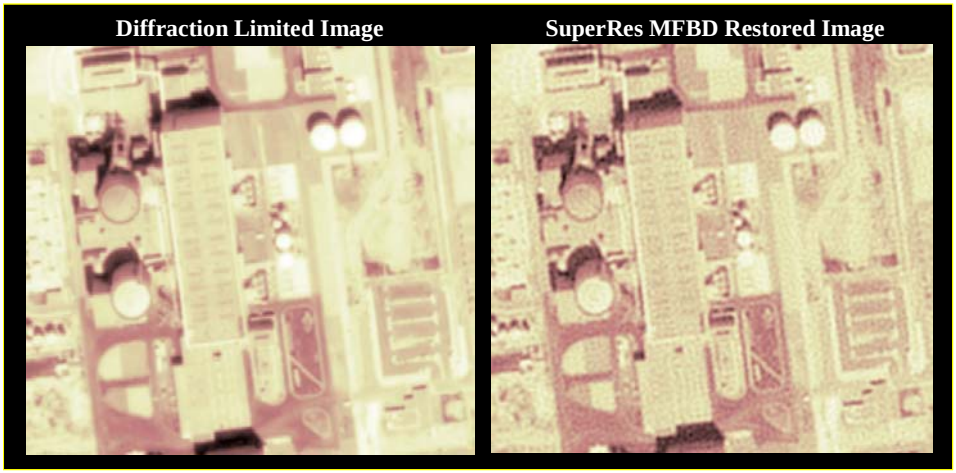

Figure 6. Comparison of the supersampling restored (superresolved) image generated from the 4x undersampled sequence of images shown in Figure 4 to the diffraction limited image shows recovery of near diffraction limited quality.

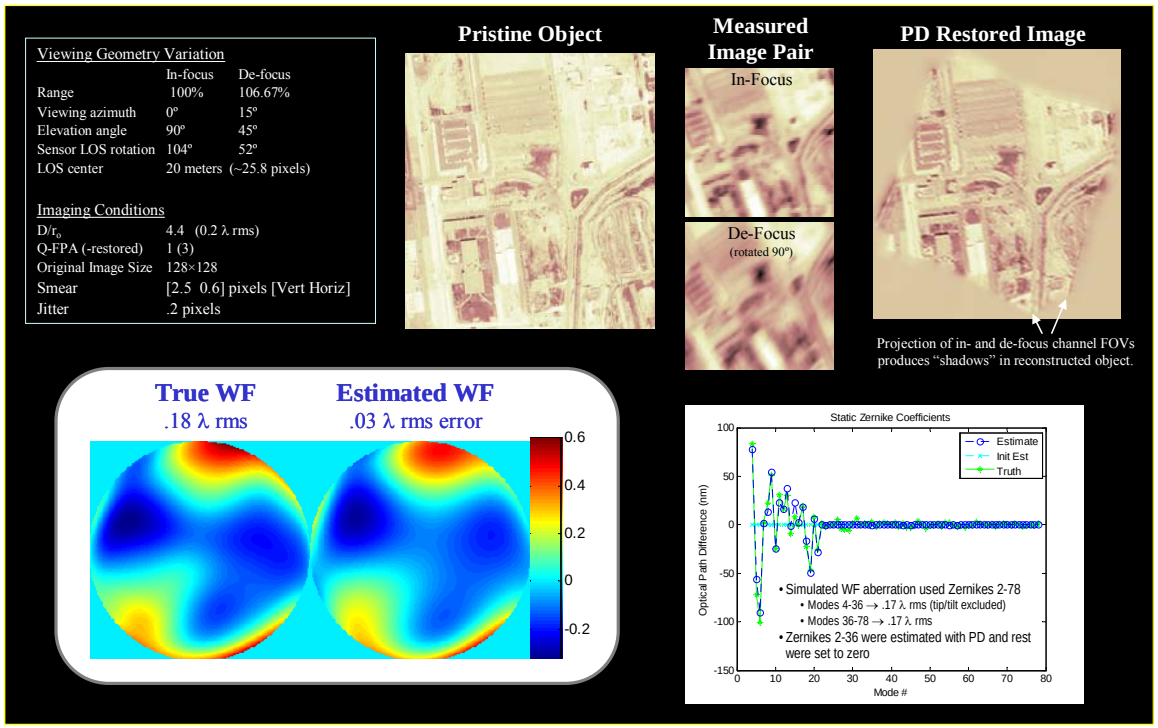

Figure 7. Accurate wavefront estimation is demonstrated using the affine geometry generalization of phase diversity to process an in- and de-focus images collected with different viewing geometries.